MOX-Report No. 104/2024

Patient-specific prediction of glioblastoma growth via reduced order modeling and neural networks

Cerrone, D.; Riccobelli, D.; Vitullo, P.; Ballarin, F.; Falco, J.; Acerbi, F.; Manzoni, A.; Zunino, P.; Ciarletta, P.

MOX, Dipartimento di Matematica
Politecnico di Milano, Via Bonardi 9 - 20133 Milano (Italy)

mox-dmat@polimi.it https://mox.polimi.it

Patient-specific prediction of glioblastoma growth via reduced order modeling and neural networks

D. Cerrone[1] D. Riccobelli[1] P. Vitullo[1] F. Ballarin[2] J. Falco[3] F. Acerbi[3]
A. Manzoni[1] P. Zunino[1] P. Ciarletta [1]

[1]MOX – Dipartimento di Matematica, Politecnico di Milano, Piazza Leonardo da Vinci 32, 20133, Milano, Italy
[2]Dipartimento di Matematica e Fisica "N. Tartaglia", Università Cattolica del Sacro Cuore, Via Garzetta 48, Brescia, 25133, Italy
[3]Department of Neurosurgery – Fondazione I.R.C.C.S. Istituto Neurologico Carlo Besta, Via Celoria 11, Milano, 20133, Italy

Abstract

Glioblastoma (GBL) is one of the deadliest brain cancers in adults. The GBL cells invade the physical structures within the brain extracellular environment with patient-specific features. In this work, we propose a proof-of-concept for mathematical framework of precision oncology enabling rapid parameter estimation from neuroimaging data in clinical settings. The proposed diffuse interface model of GBL growth is informed by neuroimaging data, periodically collected in a clinical study from diagnosis to surgery and adjuvant treatment. We build a robust and efficient computational pipeline to aid clinical decision-making based on integrating model reduction techniques and neural networks. Patient specificity is captured through the segmentation of the magnetic resonance imaging into a computational replica of the patient brain, mimicking the brain microstructure by incorporating also the diffusion tensor imaging data. The full order model (FOM) is first discretized using the finite element method and later approximated by a reduced order model (ROM) adopting proper orthogonal decomposition (POD). Trained by clinical data, we finally use neural networks to map the parameter space of GBL evolution over time and to predict the patient-specific model parameters from the observed clinical evolution of the tumor mass.

1 Introduction

Glioblastoma (GBL) is one of the deadliest types of brain cancer in adults [1]. Peculiar histological features consist of prominent cellular and nuclear atypia, numerous mitotic figures, necrosis, and microvascular proliferation. The 2021 WHO classification of central nervous system (CNS) tumors updated the diagnostic criteria introducing relevant innovations in tumor's definition, underlining the preponderant role of genetic elements compared to morphological ones [2]. GBL diagnosis is appropriate for each IDH wild-type astrocytic tumor presenting with concurrent +7/-10, EGFR amplification, or a TERT promoter mutation, even in the absence of classical high-grade histopathologic features. As the most aggressive malignant glioma, GBL has a high invasive potential and grows along white matter fibres or vessels, imitating the physical structures of the brain extracellular environment [3]. The most relevant consequence of this capability of extensive infiltration is that, despite aggressive multimodal therapy consistent in surgical resection, radiotherapy, and chemotherapy (Stupp protocol, as described in 2005), GBL invariably recurs, usually growing at the margin of the surgical cavity [4]; accordingly, prognosis remains poor with a median progression-free and overall survival times approximately of 7 and 15 months, respectively, and the five-year survival rate is approximately 5% [5]. Maximal tumor safe resection is the therapeutic cornerstone [6]: intraoperatively, GBL appears as an infiltrative mass, poorly delineated, bleeding, of increased consistency with peripheral grayish aspect and a central area of yellowish necrosis due to myelin breakdown. The ambiguous delimitation of tumor margins is one of the causes of difficult and rarely occurring complete tumor resection [7]. The recent development of technological tools such as neuronavigation, optical fluorescence imaging, intraoperative brain MRI, confocal laser endomicroscopy, and ultrasound have improved the intraoperative guidance, even they seem to be not enough to guarantee a radical resection [8, 9]. Radiologically, GBL appears as a bulky mass with heterogeneous enhancement and central necrosis; concomitantly surrounding T2/FLAIR abnormality indicates areas of vasogenic edematous, infiltrating, and non-enhancing neoplastic tissue: more than 90% of tumor recurrences will occur within this T2/FLAIR envelope and there is limited research focused on the assessment of this region and its microenvironment. The development of MR spectroscopy allowed to measure the levels of specific brain metabolites which correlate with neoplastic aggressive proliferation. PET with specific traced amino acids can further improve the radiological diagnostic accuracy, increasing the visualization of highly metabolically active tissue and differentiating these regions from edematous tissue and post-treatment tissue [10]. Artificial Intelligence (AI) has recently emerged as a prom-

ising tool to further improve the neuroradiological power of tumor detection: in particular, radiomics treats images as numerical data and extracts intricate features, eluding human observation; AI's impact could consequently extend to treatment planning for clinicians [11]. The only way forward is interdisciplinary collaboration to define the best decision-making algorithms. As stated above, the complex intratumoral heterogeneity at the genetic, biological, and functional levels, together with the tumor microenvironment is a crucial factor in making GBL extremely resistant to treatments [12, 13]. In addition, GML cells show a bursting tendency to infiltrate into the surrounding normal brain tissues of the tumor with a high complexity in tailoring surgical resection and adjuvant therapies [14]. In this context, the development of a precision in silico medicine by means of the release of increasingly updated mathematical models could play a fundamental role in describing GBL development and proliferation with a pivotal therapeutic importance [15].

The remainder of this article is organized as follows. In Section 2, we introduce the mathematical model for GBL growth based on a diffuse-interface approach, followed by the finite element formulation and the reduced order model using Proper Orthogonal Decomposition. Section 3 presents the results of the numerical simulations, including patient-specific parameter estimation through neural networks. In Section 4, we discuss a proof-of-concept application on clinical data, demonstrating the potential of our framework. Finally, Section 5 concludes the paper with a summary of the key findings and directions for future research.

2 Model

In this section, we introduce a diffuse interface model and a numerical framework designed for predicting the patient-specific GBL growth from neuroimaging data. Although certain information, such as the geometry of the patient's brain and local brain fiber orientation and physiological brain data, can be derived from imaging techniques as discussed in the Appendix A.2, the cancer phenotype exhibits considerable variability and the prediction of its evolution is difficult and requires a patient-specific approach. Hence, we put forward a mathematical model alongside a machine learning-based approach to estimate the parameters pertaining to the patient's tumor.

2.1 Diffuse interface model of GBL growth

The brain tissue is modeled as a mixture of a cellular phase, representing the tumor, and a liquid phase, which describes the healthy host tissue. In the framework of mixture theory, at the mesoscopic level, every material point of the mixture represents a reference volume occupied by volume fractions of the interacting phases [16]. Let $\Omega \subset \mathbb{R}^3$ be the domain representing the brain. We can define the spatial concentration of each constituent at the instant of time t at each point $\mathbf{x} \in \Omega$. Specifically, we introduce the volume fraction of the tumor $\phi_c(\mathbf{x}, t)$ and the volume fraction of the healthy tissue $\phi_l(\mathbf{x}, t)$, such that $\phi_c(\mathbf{x}, t), \phi_l(\mathbf{x}, t) \in [0, 1]$. We assume that the mixture is fully saturated, so that $\phi_c + \phi_l = 1$ at each point of the mixture and at any time $t \in [0, T]$. From this, it is possible to define a new variable $\phi := \phi_c - \phi_l$ that assumes value 1 where there are only tumor cells and -1 on healthy areas.

We also assume that the two phases have a density roughly equal to the one of water γ. Let $\mathbf{v}_c$ and $\mathbf{v}_l$ be the velocities of the cellular and the healthy phase, respectively. The following form of the mass balance holds true

$$\frac{\partial \phi_i}{\partial t} + \nabla \cdot (\phi_i \mathbf{v}_i) = \frac{\Gamma_i}{\gamma} \quad i \in \{c, l\}, \tag{1}$$

where Γ_c and Γ_l denote the mass source terms per unit volume of the two fractions. The average velocity of the mixture can be defined as $\mathbf{v} = \phi_c \mathbf{v}_c + \phi_l \mathbf{v}_l$.

To enforce the incompressibility of the whole mixture, we prescribe that $\Gamma_c = -\Gamma_l$. Indeed, if we sum the two continuity equations in (1), we obtain

$$\nabla \cdot (\phi_c \mathbf{v}_c + \phi_l \mathbf{v}_l) = \nabla \cdot \mathbf{v} = 0.$$

By subtracting the two continuity equations (1) we obtain

$$\frac{\partial (\phi_c - \phi_l)}{\partial t} + \nabla \cdot (\phi_c \mathbf{v}_c - \phi_l \mathbf{v}_l) = \frac{\Gamma_c - \Gamma_l}{\gamma} \tag{2}$$

Let $\mathcal{J}_c$ and $\mathcal{J}_l$ be the mass fluxes of the two phases with respect to the mixture velocity $\mathbf{v}$, defined as

$$\mathcal{J}_c = \gamma \phi_c (\mathbf{v}_c - \mathbf{v}), \tag{3}$$

$$\mathcal{J}_l = \gamma \phi_l (\mathbf{v}_l - \mathbf{v}). \tag{4}$$

By introducing $\mathcal{J} = \frac{1}{\gamma}(\mathcal{J}_c - \mathcal{J}_l)$ and subtracting Eqs. (3)-(4), we get

$$\phi_c \mathbf{v}_c - \phi_l \mathbf{v}_l = \phi \mathbf{v} + \mathcal{J}. \tag{5}$$

We can use Eq. (5) to rewrite Eq. (2) as follows

$$\frac{\partial \phi}{\partial t} + \nabla \cdot (\phi \mathbf{v}) + \nabla \cdot \mathcal{J} = \frac{\Gamma}{\gamma} \quad \text{with} \quad \Gamma = \Gamma_c - \Gamma_l.$$

We assume that the mixture is very viscous and free of external forces. We use an approach based on non-equilibrium thermodynamics to determine a constitutive law for the mass fluxes. We take the following expression of the Landau free energy:

$$F(\phi) = \int_{\mathcal{B}_t} \left(\kappa \Psi(\phi) + \frac{\epsilon^2}{2} |\nabla \phi|^2 \right) d\mathcal{B}_t, \tag{6}$$

κ is the brain Young modulus, ϵ defines the interfacial tension, and $\mathcal{B}_t$, i.e. the region occupied by the brain, is assumed to be with fixed boundaries over time. Therefore, from now on we omit the time specification and we refer to the domain with the symbol $\mathcal{B}$. The two addends inside the integral in Eq. (6) represent the mixing energy density and the interface energy arising from the interaction between the two different phases, respectively [17].

In this specific case, we take as cell-cell interaction potential $\Psi(\phi)$ a function with a double-well shape, such that its minima are attained in $\phi = 1$ and $\phi = -1$, corresponding to the two pure phases. A simple admissible choice is given by

$$\Psi(\phi) = \frac{1}{4}(1 - \phi^2)^2. \tag{7}$$

By following Fick's law, we postulate $\mathcal{J}$ to be proportional to the gradient of a chemical potential $\mu = \frac{\delta F(\phi)}{\delta \phi}$, where δ is the Gâteaux functional derivative [18]. Thus, we assume that

$$\mathcal{J} = -\frac{1}{M_0} \mathsf{T} \nabla \mu$$

where M_0 is a friction coefficient, while T represents the preferential motility tensor [19].

To close the model, we prescribe that Γ depends on the local oxygen concentration by setting

$$\Gamma = \Gamma(\phi, n) = \nu \gamma \Big(\frac{n}{n_s} - \delta \Big) h(\phi). \tag{8}$$

Here, ν is the tumor cell proliferation rate, n represents the local concentration of oxygen, n_s is a physiological value for the oxygen concentration in brain tissue, δ is the hypoxia threshold, and $h(\phi)$ is a function that allows the proliferation in the natural range of ϕ.

The function h should be constitutively prescribed. It should suppress the proliferation of tumor cells when $\phi = -1$, i.e. when we are in the correspondence of the absence of the tumor. A possible choice for h is given by

$$h(\phi) = \max \left(\min \left(1, \frac{1}{2}(1 + \phi) \right), 0 \right)$$

The dynamics of oxygen concentration are modeled by means of a reaction-diffusion equation, where D is the diffusivity tensor of the nutrient, S_n is the *oxygen supply rate* and δ_n is the *oxygen consumption rate*. Accordingly, following [18, 20], the system of partial differential equations describing the dynamics of GBL growth is composed of a Cahn-Hilliard equation and a reaction-diffusion equation for the nutrient concentration

$$\begin{cases} \dfrac{\partial \phi}{\partial t} = \nabla \cdot \Big(\dfrac{1}{M_0} \mathsf{T} \nabla \mu \Big) + \nu \, (\hat{n} - \delta) \, h(\phi), \\ \mu = \kappa \Psi'(\phi) - \epsilon^2 \Delta \phi, \\ \dfrac{\partial \hat{n}}{\partial t} = \dfrac{S_n}{3} (1 - \hat{n}) \, (2 - \phi) \\ \qquad\quad + \nabla \cdot (\mathsf{D} \nabla \hat{n}) - \delta_n \hat{n} h(\phi). \end{cases} \tag{9}$$

where the auxiliary variable μ represents the chemical potential, while $\hat{n} = n/n_s$. The parameters are the tumor cells proliferation rate ν, the tumor interphase friction M_0, the brain Young modulus κ, the diffuse interfacial energy ϵ, the oxygen concentration in vessels n_s, the hypoxia threshold δ, the oxygen consumption rate δ_n and the oxygen supply rate S_n. Their biological range is collected in Table 1. The tensors D and T can be extracted from patient's imaging data following the procedure detailed in Appendix A.2. Finally, we enforce a homogeneous Neumann boundary condition for each physical variable at the brain boundary. We refer to the task of finding the solution to Eq. (9) as the direct problem, in what follows we propose a strategy to construct a reduced order model which allows for a faster computation of the numerical solution.

2.2 Finite element formulation of the full order model

First, we computationally solve Eq. (9) using the finite element method. In such a way, we obtain a discrete counterpart of the model proposed in Eq. (9). We refer to such a discrete problem as the *full order model* (FOM) on a discrete partition $\mathcal{T}_h$. Then, we divide the temporal interval $[0, T]$ into N discrete subintervals $\Delta t = T/N$. The j-th simulation time-point $t^j = j\Delta t$ with $j = 0, ..., N$. Next, we introduce the finite element space $V_h = \Big\{ \chi \in C^0(\Omega) : \chi|_K \in \mathbb{P}^1(K) \quad \forall K \in \mathcal{T}_h \Big\} \subset H^1(\Omega)$, which is the space of continuous polynomial functions of degree 1 ($\mathbb{P}^1$) when restricted on each element K. V_h is a subset of the Hilbert space $H^1(\Omega)$ that contains $L^2(\Omega)$ functions whose first weak derivative is in $L^2(\Omega)$ too.

Thus, given the initial data $(\phi_h^0, \hat{n}_h^0) \in V_h \times V_h$ we

Symbol	Range of values	Ref.
M_0	$1.38 \times 10^3 - 5.03 \times 10^3\,\mathrm{Pa\,d\,mm^{-2}}$	[21]
ν	$1.2 \times 10^{-2} - 0.5\,\mathrm{d}^{-1}$	[22, 23]
S_n	$1 \times 10^3 - 1 \times 10^5\,\mathrm{d}^{-1}$	[24]
δ_n	$1 \times 10^3 - 1 \times 10^5\,\mathrm{d}^{-1}$	[23]
κ	$1.06 \times 10^2 - 1.53 \times 10^3\,\mathrm{Pa}$	[25]
δ	$0.1 - 0.33$	[26]

Table 1: *Biological range found in literature for the parameters of the model.*

obtain the following discrete problem:

$$\begin{cases} \left(\dfrac{\phi_h^{j+1}-\phi_h^j}{\Delta t},\varphi_h\right) = -\dfrac{1}{M_0}\left(\mathsf{T}\nabla\mu_h^{j+1},\nabla\varphi_h\right) + \\ \qquad\qquad +\nu\left(\left(\hat{n}_h^{j+1}-\delta\right)h\left(\phi_h^j\right),\varphi_h\right) \\ \left(\mu_h^{j+1},v_h\right) = \epsilon^2\left(\nabla\phi_h^{j+1},\nabla v_h\right) + \kappa\left(\Psi_c'\left(\phi_h^{j+1}\right),v_h\right) + \\ \qquad\qquad +\kappa\left(\Psi_e'\left(\phi_h^j\right),v_h\right) \\ \left(\dfrac{\hat{n}_h^{j+1}-\hat{n}_h^j}{\Delta t},q_h\right) = -\left(\mathsf{D}\nabla\hat{n}_h^{j+1},\nabla q_h\right) + \\ \qquad\qquad +S_n\left(\left(1-\hat{n}_h^{j+1}\right)\dfrac{1}{3}\left(2-\phi_h^j\right),q_h\right) + \\ \qquad\qquad -\delta_n\left(\hat{n}_h^{j+1}h\left(\phi_h^j\right),q_h\right) \end{cases}$$

where $(\cdot,\cdot)$ denotes the standard L^2 inner product over Ω. As suggested in [27] we prescribe the following splitting for the Cahn-Hilliard potential to ensure the gradient stability of the scheme:

$$\Psi_c\left(\phi_h^{j+1}\right) = \frac{\left(\phi_h^{j+1}\right)^4+1}{4}, \quad \Psi_e\left(\phi_h^j\right) = -\frac{\left(\phi_h^j\right)^2}{2}.$$

Decomposing the potential in such a way, i.e. in a convex term Ψ_c that we can treat with an implicit scheme and a concave term Ψ_e that is treated with an explicit scheme, ensures the solution to be stable over time [28].

2.3 Reduced order model

Solving the FOM requires a huge amount of computational resources and time. Aiming at constructing an effective procedure to solve the inverse problem of patient-specific parameter identification from neuroimaging data, we resort to a *reduced order model* (ROM) based on linear projections as a robust and more efficient solution strategy. The basic idea is to construct a reduced basis (RB) space for the approximation of the discrete solution manifold. Starting from the system Eq. (9), we perform a Proper Orthogonal Decomposition (POD) [29, 30] on a set of FOM solutions, named *snapshots*.

The construction of a basis for the final reduced order space consists of two similar steps. We first perform a Singular Value Decomposition (SVD) over the snapshot matrix associated with the variable $f = \{\phi, \mu, n\}$ associated with a particular choice of the parameters $\mathcal{P}_k = [\nu_k, M_{0l}, \kappa_k, \delta_k, \delta_{nk}, S_{nk}]$ at a given instant of time. Specifically, the matrix columns are the nodal values of the solution at a specific time-step

$$F_f^1 = [f_k^0, ..., f_k^N],$$

where $N+1$ is the number of time-steps. By applying SVD on F_f^1, we obtain a basis $\left\{\xi_{kl}^f\right\}_{l=1,...,N_{\mathrm{POD}}^k}$ from each set of parameters $\mathcal{P}_k$, where N_{POD^k} is chosen such that information that the POD basis should cover, indicated as $ic \in (0,1]$, is about $ic = 0.95$ for each variable. We denote by M the cardinality of the set of parameters, so that $k = 1, \ldots, M$. Until this point, the bases contain most of the information on the evolution of the tumor through time for a specific set of parameters. Then, we perform another SVD, this time starting from the matrix collecting the M bases obtained in the previous step, i.e.

$$F_f^2 = \left[\xi_{11}^f, ..., \xi_{1N_{\mathrm{POD}}^1}^f, ..., \xi_{M1}^f, ..., \xi_{MN_{\mathrm{POD}}^M}^f\right].$$

The final result is a basis $\left\{\xi_l^f\right\}_{l=1,...,N_{\mathrm{POD}}}$ of the reduced order space for each variable $f = \{\phi, \mu, n\}$. A similar strategy has been used e.g. in [31–34] to generate the POD basis for models depending on both time and parameters.

Let ξ_i^f be the generic element of the reduced basis of the physical variable f, we can write

$$\phi_h^t = \sum_{i=1}^{N_{\mathrm{POD}}} a_{\phi i}^t \xi_i^\phi,\ \mu_h^t = \sum_{i=1}^{N_{\mathrm{POD}}} a_{\mu i}^t \xi_i^\mu,\ \hat{n}_h^t = \sum_{i=1}^{N_{\mathrm{POD}}} a_{ni}^t \xi_i^n,$$

where N_{POD} is the cardinality of the reduced basis. N_{POD} is chosen such that information that the POD basis should cover $ic \in (0,1]$ is about $ic = 0.95$ for each variable.

To sum up, the steps that we perform for each phase are [35]:

- prescribe the amount of required information that the POD basis should cover $ic \in (0,1]$;

- compute the trace $tr(F_f^t F_f)$ of the correlation matrix $F_f^t F_f = (f^m, f^l)_{ml}$;
- evaluate the pair eigenvalues-eigenvectors

$$\{\lambda_{fi}, v_f^i\}_{i=1,...,N_f^{\text{POD}}}$$

of $F_f^t F_f$;
- $N_f^{\text{POD}} = \min\left\{m, \left(\sum_{i\leq m}\lambda_i\right)/tr(F^tF) \leq ic\right\}$, that is the number of elements in the basis, is set;
- $N^{\text{POD}} = \max\left\{N_\phi^{\text{POD}}, N_\mu^{\text{POD}}, N_n^{\text{POD}}\right\}$
- set $\zeta_s^f = \frac{1}{\sqrt{\lambda_{fs}}}\sum_j (v_f^s)_j f^j$ where $(1 \leq s \leq N^{\text{POD}})$.

Since the model in Eq. (9) is non-linear, a classical POD-Galerkin method requires the projection of the non-linear operators. When a general non-linearity is present, the cost to evaluate the projected nonlinear function still depends on the dimension of the original system, resulting in simulation times that hardly improve over the original system. A possible approach to overcome this issue is the usage of hyper-reduction techniques, such as those based on a greedy algorithm using DEIM interpolation, as proposed in [36]. In this work, an alternative approach, exploiting neural networks, is preferred to approximate the RB coefficients in a non-intrusive framework, resorting only on the simulation data and without manipulating directly the governing equations with Galerkin projections as with the classical intrusive hyper-reduction techniques.

The reduction of the problem to a few degrees of freedom, equal to the dimensionality of the reduced space N_{POD} and corresponding to the coefficients of the RB, makes it possible to train a simple neural network that maps the parameter space onto the space of the RB coefficients, a method usally referred to as the POD-NN approach [37]. Given a set of parameters $\mathcal{P} = [\nu, M_0, \kappa, \delta, \delta_n, S_n]$ of cardinality N_P, along with a temporal step t, we train the neural network $\mathbf{NN}_\phi : \mathbb{R}^{N_\mathcal{P}+1} \rightarrow \mathbb{R}^{N_{\text{POD}}}$ to compute the coefficients $\{a_{t,i}^\phi\} \in \mathbb{R}^{N_{POD}}$ for the RB of the tumor concentration variable ϕ. Following the procedure presented in [37], $\mathbf{NN}_\phi$ is an approximation of the function that map points $[\nu, M_0, \kappa, \delta, \delta_n, S_n, t]$, which corresponds to a tumor distribution at a given instant t, to the space of coefficients $\{a_{t,i}^\phi\}_{i=1,...,N_{POD}}$ of the projected solution in the ROM space at the same time instant. We choose not to make ε vary since it is related to the thickness of the diffusive interface that is fixed a priori, while the tensors T and D are extracted from neuroimaging data, as described in the Appendix.

3 Results

3.1 Surrogate approach to estimate patient-specific parameters from neuroimaging data

We propose in the following a numerical pipeline to infer the patient-specific parameters of GBL growth from the observed tumor distribution at two different instants of time, given by the clinical follow-up protocol summarized in the Appendix A.1. In the following, we refer to the identification of the patient-specific parameters given the observed distributions of the tumor as the *inverse problem*. Also for this purpose, we exploit surrogate neural network techniques to approximate the solutions. An illustration of the proposed computational pipeline is presented in Fig. 1

In order to solve the inverse problem of estimating the patient-specific parameters from the observed tumor distribution given by two instants of time from clinical follow-up, we construct a second neural network. In this case, the trained neural network is a map $\mathbf{NN}_{\text{inv}} : \mathbb{R}^{2N^{\text{POD}}} \rightarrow \mathbb{R}^{N_\mathcal{P}}$ that takes as inputs two tumor distributions, identified with their projection coefficients over the reduced basis, and gives the set of parameters as the output, i.e.

$$(\nu, M_0, \kappa, \delta, \delta_n, S_n) = \mathbf{NN}_{\text{inv}}\left(a_{\phi 1}^{t_0}, ..., a_{\phi N_{\text{POD}}}^{t_0}, a_{\phi 1}^{t_1}, ..., a_{\phi N_{\text{POD}}}^{t_1}\right)$$

where t_0 and $t_1 = t_0 + (20\,\text{days})$ represent the time interval that elapses from the first and second MRI. We choose the weighted sum as the propagation function, the LeakyReLU as the activation function and just the identity for the output function. Moreover, the loss function used is the mean squared error.

3.2 Proof-of-concept

We finally build a proof-of-concept by image segmentation of the MRI and DTI data from a clinical case, as shown in Fig. 2. The details of the clinical and radiological protocols are summarized in the Appendix A.1. This realistic brain-shaped mesh has 32293 vertices and 196778 tetrahedral elements. A mesh refinement is performed in the neighborhood of the initial placement of the tumor. For each simulation, a piecewise linear basis function is chosen, so that the degrees of freedom of the solution correspond to the number of vertices. For the numerical solution of the FOM, we rely on a HPC cluster (Intel® Xeon® Processor E5-2640 v4, 20 cores, 64 GB RAM). The overall implementation framework exploits the functionalities given by the platform `FEniCSx`, a popular open-source environment for solving partial differential equations.

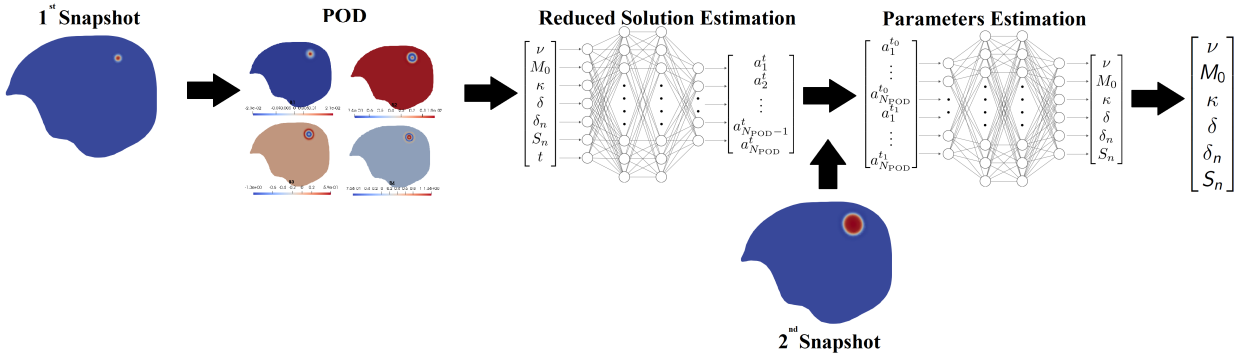

Figure 1: *Representation of the computational pipeline. The geometry and the distribution of the tumor is known at for $t = t_0$. From this datum, we perform the POD and get the reduced order solution estimation for the direct problem (POD-NN procedure). Given the distribution of the grown tumor at $t = t_1 = t_0 + 20$ days, we train a neural network to solve the inverse problem estimating the patient-specific parameters.*

The implementation of the used code heavily relies on two of its components: `dolfinx`, a C++/Python library providing data structures and algorithms for finite element meshes, automated finite element assembly, and numerical linear algebra, and the Unified Form Language `UFL` which is a domain-specific language for declaration of finite element discretization of variational forms. The construction of the ROM basis is obtained through `RBniCSx`, a library useful to implement reduced order modeling techniques. The neural network is implemented in Python using `PyTorch`. As a minimization procedure for the loss function we have used the L-BFGS algorithm [38].

For training the neural network of the direct problem, we draw parameters out of the biological range exhibited in Tab. 1.

To obtain adequate accuracy the training for the direct POD-NN, we construct a data set from numerical simulations obtained by 750 different sets of parameters. Using 60 temporal steps, each of them representing 0.5 days, we finally get $N^{\text{dir}}_{\text{Data}} = 45000$ input-output pairs. This data set is split into a training set with $N^{\text{dir}}_{\text{train}} = 33000$ elements and a test set with $N^{\text{dir}}_{\text{test}} = 12000$ elements.

We perform FOM computations with $M = 64$ different sets of parameters, to build up a representative basis that can retain most of the energy present in all of the original variables. In this case, a basis with $N_{\text{POD}} = 40$ elements was big enough to have an acceptable error between the FOM solution and the POD-Galerkin one, as shown in Fig. 3.

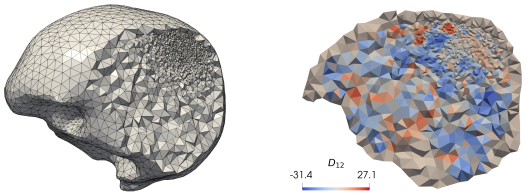

Figure 2: *A representation of the computational domain (left) and of a component of the diffusion tensor* D *(in* $\text{mm}^2\,\text{d}^{-1}$*) extracted from the DTI data (right).*

From this, it is possible to create a data set for the neural networks for the map of the direct problem $\mathbf{NN}_\phi$ that relies on 750 different possible evolutions of the tumor starting from the same initial condition $\phi_0(x,y,z) = 2e^{-100((x-193)^2+(y-308)^2+(z-30)^2)} - 1$ where spatial quantities are measured in *mm*. The results of the training in terms of mean squared error over epochs are shown in Fig. 4.

Since the POD-Galerkin solution is computationally demanding due to the absence of hyper-reduction techniques (see Section 2.3), as illustrated in Fig. 5, we opt to simulate the FOM first and subsequently project onto the reduced basis. Once training is complete, the POD-NN achieves a computational speed-up of approximately 200 times compared to the FOM solver, see Fig. 5.

Given the distributions of the tumor at two sufficiently distant instants of time, in order to discriminate between different possible evolutive scenarios with more accuracy, we can produce a data set whose input-output pairs are formed by the vector containing the coefficients of the projections of the tumor distribution over the RB and the patient-specific parameters. To train the inverse neural network, denoted by **NN**inv, we extract twenty pairs of tumor distributions, each separated by a distance of twenty days, for each of the 750 parameter sets. This results in a total of $N^{\text{inv}}_{\text{data}} = 15000$ input-output pairs. These are then split into a training set containing $N^{\text{inv}}_{\text{train}} = 11000$ elements and a test set with $N^{\text{inv}}_{\text{test}} = 4000$ elements. The mean squared errors over epochs for the neural network $\mathbf{NN}_{\text{inv}}$, computed for normalized over the biological range parameters, are shown in Fig. 4. Although this result appears to be non-optimal in order to catch the exact parameter of a patient (the com-

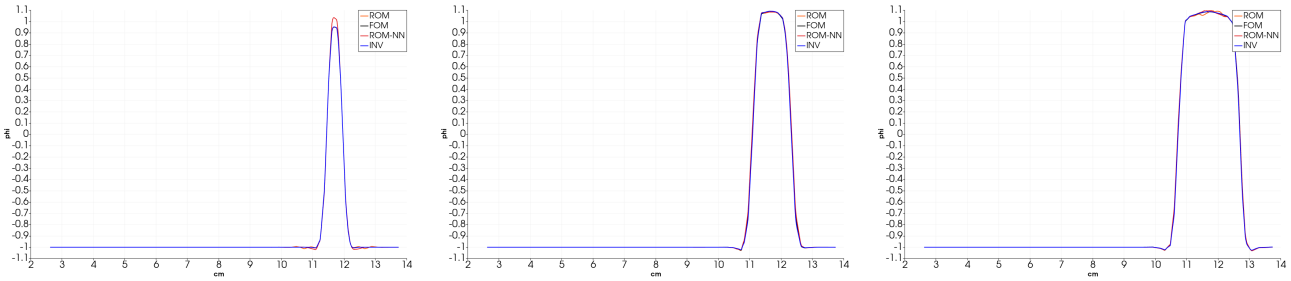

Figure 3: *Plot of the solution ϕ within a fixed sagittal plane intersecting the tumor centroid at t= 0 (left), 15 (center), 30 days (right). Solid lines indicate the FOM solution (black), the POD-Galerkin solution (orange), the POD-NN solution (red), and the FOM solution obtained using the parameter obtained in the inverse problem (blue).*

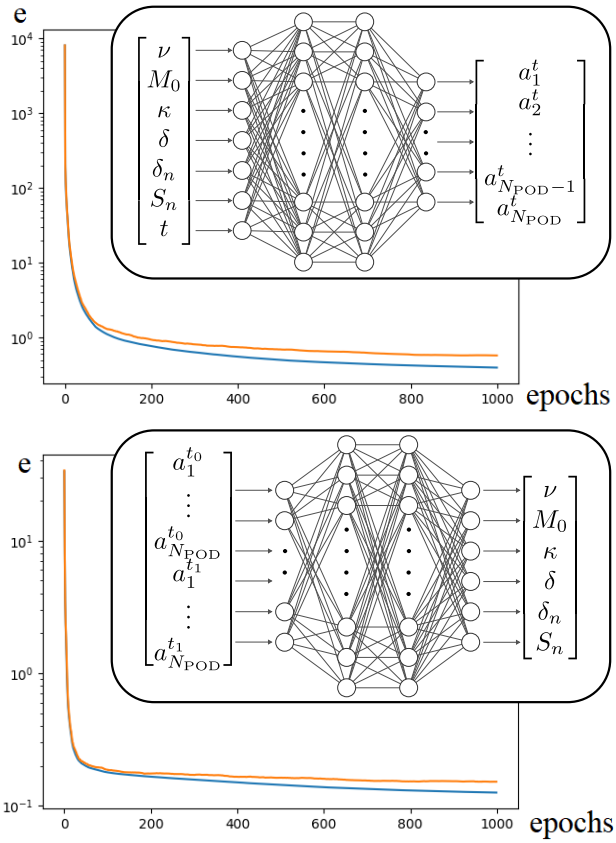

Figure 4: *Absolute (top) and relative (bottom) mean squared error* **e** *over the epochs in the training of the direct (top) and the inverse (bottom) neural networks. The solid lines indicate the errors over the training set (blue) and over the test sets (orange).*

puted error is about 15%, see the bottom panel of Fig. 4), the simulations performed show that the specific behaviour is actually well captured.

Giving as input the distribution of the tumor starting from the parameters

$$\begin{aligned} &M_0 = 3860.7\,\mathrm{Pa\,d\,mm^{-2}}, && \delta_n = 21\,041\,\mathrm{d^{-1}}, \\ &\nu = 0.356\,\mathrm{d^{-1}}, && \kappa = 700.4\,\mathrm{Pa}, \\ &S_n = 41\,978\,\mathrm{d^{-1}}, && \delta = 0.24. \end{aligned} \tag{10}$$

we obtain the following result

$$\begin{aligned} &M_0 = 3950.4\,\mathrm{Pa\,d\,mm^{-2}}, && \delta_n = 25\,142\,\mathrm{d^{-1}}, \\ &\nu = 0.369\,\mathrm{d^{-1}}, && \kappa = 776.8\,\mathrm{Pa}, \\ &S_n = 36\,982\,\mathrm{d^{-1}}, && \delta = 0.25. \end{aligned} \tag{11}$$

In Fig. 5 (top) the evolution of the tumor with the actual set of parameters and the evolution with the predicted set is exhibited. As we can see in Fig. 5 (right, bottom), the volume fraction is well-tracked over time entailing a good estimation both in terms of tumor morphology. The elapsed time for the estimation of the parameters is of the order of seconds (Fig. 5) since it only requires the evaluation of the trained map at a specific point given by the projected tumor distributions onto the reduced basis.

4 Conclusions

In this work, we presented a patient-specific predictive framework for GBL growth using a ROM constructed via POD and coupled with neural networks. By integrating medical imaging data with a diffuse-interface mathematical model, we introduced a robust computational approach for estimating key patient-specific parameters and predicting tumor growth with a reduction of the computational time by the 99%. The proposed methodology efficiently reduces computational costs while maintaining high accuracy in the predictions of the tumor growth evolution (96% in forecasting the final volume, see Fig. 5), making it a viable tool for clinical applications.

Our results show that this framework can effectively solve both the direct and inverse problems of GBL growth. Once the neural network is trained, patient-specific predictions can be made within seconds, underscoring the relevance of this approach for real-time therapeutic planning in clinical settings.

Nonetheless, there are still some limitations to be addressed. Future developments will aim at refining the mathematical model to incorporate crucial

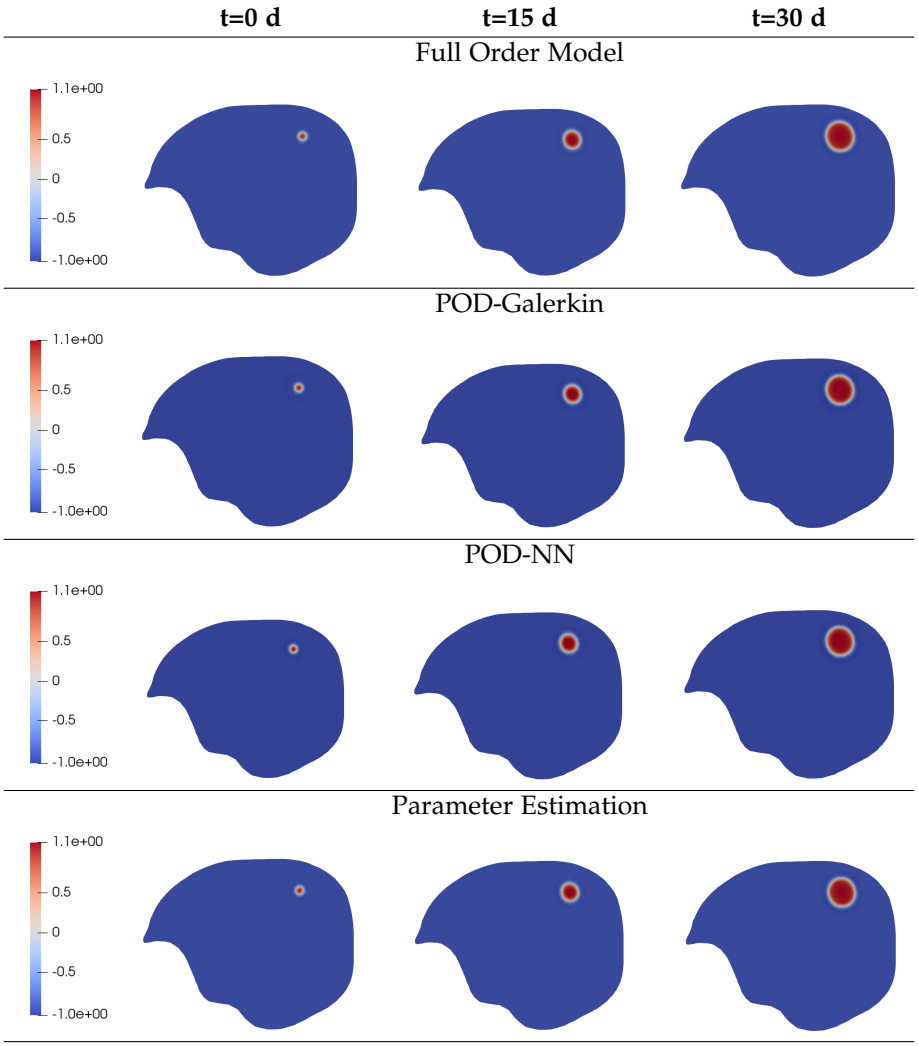

Method	Elapsed Time
FOM	920 s
POD-Galerkin	5190 s
POD-NN	5 s

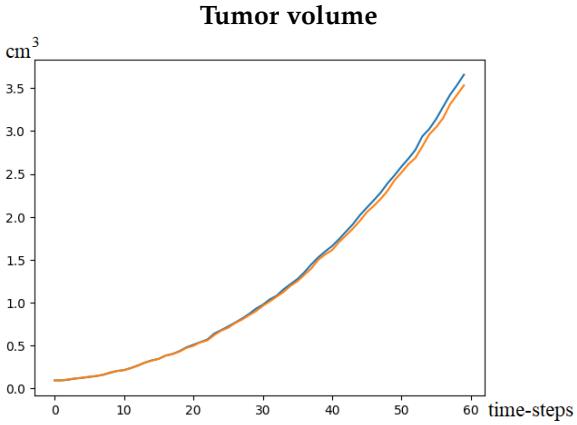

Figure 5: *FOM, POD-Galerkin, POD-NN, and patient-specific FOM solutions of a GBL concentration ϕ at $t = 0, 15, 30$ days (top) and corresponding computational times (bottom,left). Volume fraction of tumor over time (bottom, right). The parameters used in the FOM and POD-Galerkin models are given by Eq.* (10)*, while the results obtained with the parameters estimated by the inverse neural network are given by* (11)*. The FOM evolution is given in orange, and the predicted one in blue.*

features such as phenotype variability and treatment responses [39], the coupling between tumor solid mechanics and growth [40–42], as well as enhancing the model's generalization to different initial conditions and mesh geometries without the need for retraining the networks for each patient [43–45].

In conclusion, this study represents a promising step towards the development of a precision medicine tool for GBL management, with significant potential to improve clinical outcomes by enabling faster and

more personalized computational predictions in real-world settings.

A Details of the medical protocol and neuroimaging techniques

A.1 Clinical protocol

This study is part of a collaboration program between Foundation IRCCS Neurological Institute Carlo Besta, Department of Neurosurgery and Neuroradiology, and Politecnico di Milano, MOX – Modeling and Scientific Computing, Department of Mathematics. At a hospital stage, we started a prospective observational trial, named GLIOMATH (GLIOblastoma MATHematics), enrolling patient with GBL submitted to surgical removal or biopsy, adjuvant therapy and follow-up based on normal clinical practice, in which specific MRI data for each patient were used as input data building a personalized virtual environment. The study was conducted according to the guidelines of the Declaration of Helsinki, and approved by the Ethics Committee of Fondazione Istituto Neurologico Carlo Besta (protocol code GlioMath, nr. 49/2016; date of approval: 13 July 2016). Patients older than 18 years old with suspected, newly diagnosed, untreated GBL and eligible for surgical removal or biopsy of their lesion were considered for participating in our trial; exclusion criteria were inability to give consent due to cognitive deficits or language disorders, or, for women, pregnancy or lactation. The patients were enrolled in a prospective observational study; the evaluation was based on the normal clinical practice [46]. All patients underwent neurological examination, preoperative volumetric MRI including DTI (3 Tesla MRI scan – Philips), and recording of concomitant medications. Patients were scheduled for surgical removal or biopsy as judged by the surgeon; in both cases, the procedures were performed in a standard manner, with any surgical tools as preferred by the operating surgeon, and neurophysiological monitoring when necessary. The histopathological and molecular analysis of the tumor samples were performed according to the 2016 or 2021 WHO classification of CNS tumors [47]. Clinical and radiological post-operative examination were carried out the usual institutional practice. The early clinical evaluation included neurological examination and volumetric contrast-enhanced MRI for estimation of extent of resection, within 72 hours from the surgical intervention. The protocol for early post-operative MRI was the same as performed in preoperative setting without the DTI, that was excluded due to the possibility of artifacts caused by the presence of air in the surgical cavity; the following radiological exams, performed every two months, were performed according to the same protocol of preoperative MRI with DTI. All patients, upon confirmation of histologic diagnosis of GBL, were offered adjuvant radio- and chemotherapy, according to the Stupp protocol and tailored on the basis of patient age, performance status and methylation status of MGMT gene promoter, according to the EANO guideline [48]. The surgical and trial databases of the above mentioned study have been collected anonymously for the scientific purposes; written informed consent was obtained for each case. Exclusively anonymized neuroradiological data were employed for the secondary phase of the study consisting in developing of a multi-scale mathematical model and simulating GBL invasion from the patient-specific data collected from MRI studies.

A.2 Neuroimaging acquisition and segmentation

The radiological protocol included volumetric axial whole brain T1-weighted MRI at $1\,mm \times 1\,mm \times 1\,mm$ spatial resolution and volumetric axial whole brain T1-weighted MRI at same spatial resolution after paramagnetic contrast administration, useful for illustrating the structural anatomy of the patient's brain and to calculate the total volume of tumor extension after segmentation procedure; axial whole brain 3D-FLAIR image at 1 mm × 1 mm × 1 mm spatial resolution, useful to delineate the outline of the tumor and peri-tumor rim by suppressing signal from cerebrospinal fluid. A set of 147 diffusion-weighted images DTI at 2 mm × 2 mm × 2 mm spatial resolution with anterior–posterior phase encoding direction with different b-value was finally acquired; all diffusion-sensitising directions were sampled uniformly on the hemisphere and an additional B0 image was acquired with reversed phase encoding direction, as posterior-anterior encoding, for helping in geometric distortion correction. The images obtained through MRI are segmented using the software 3D Slicer and the mesh is generated using the VMTK library. Finally, the DTI data are then analyzed using the library ANIMA[1] to reconstruct the tensors D and T.

Acknowledgements

This work was partly supported by MUR through the grants PRIN 2020 Research Project MATH4I4 and Dipartimento di Eccellenza 2023-2027. DR and FB have been partially supported by the PRIN 2022 project *Mathematical models for viscoelastic biological matter*,

[1] `https://github.com/Inria-Empenn/Anima-Public`

Prot. 202249PF73 – Funded by European Union - Next Generation EU – Italian Recovery and Resilience Plan (PNRR) - M4C1, CUP D53D23005610001 for DR, CUP J53D23003590008 for FB.

References

[1] P. Y. Wen et al. 'Glioblastoma in adults: a Society for Neuro-Oncology (SNO) and European Society of Neuro-Oncology (EANO) consensus review on current management and future directions'. *Neuro-Oncology* 22.8 (2020), pp. 1073–1113.

[2] D. N. Louis et al. 'The 2021 WHO Classification of Tumors of the Central Nervous System: a summary'. *Neuro-Oncology* 23.8 (2021), pp. 1231–1251.

[3] T. S. Deisboeck et al. 'Pattern of self-organization in tumour systems: complex growth dynamics in a novel brain tumour spheroid model'. *Cell Proliferation* 34.2 (2001), pp. 115–134.

[4] R. Stupp et al. 'Radiotherapy plus Concomitant and Adjuvant Temozolomide for Glioblastoma'. *New England Journal of Medicine* 352.10 (2005), pp. 987–996.

[5] A. Omuro and L. M. DeAngelis. 'Glioblastoma and Other Malignant Gliomas: A Clinical Review'. *JAMA* 310.17 (2013), p. 1842.

[6] T. J. Brown et al. 'Association of the Extent of Resection With Survival in Glioblastoma: A Systematic Review and Meta-analysis'. *JAMA Oncology* 2.11 (2016), p. 1460.

[7] M. Rivera et al. 'Updates on Surgical Management and Advances for Brain Tumors'. *Current Oncology Reports* 23.3 (2021).

[8] C. Cavallo et al. 'The utilization of fluorescein in brain tumor surgery: a systematic review'. *Journal of Neurosurgical Sciences* 62.6 (2018).

[9] S. L. Hervey-Jumper and M. S. Berger. 'Maximizing safe resection of low- and high-grade glioma'. *Journal of Neuro-Oncology* 130.2 (2016), pp. 269–282.

[10] K. Petrecca et al. 'Failure pattern following complete resection plus radiotherapy and temozolomide is at the resection margin in patients with glioblastoma'. *Journal of Neuro-Oncology* 111.1 (2012), pp. 19–23.

[11] C. Chirica et al. 'One Step Forward—The Current Role of Artificial Intelligence in Glioblastoma Imaging'. *Life* 13.7 (2023), p. 1561.

[12] J.-M. Lemée, A. Clavreul and P. Menei. 'Intratumoral heterogeneity in glioblastoma: don't forget the peritumoral brain zone'. *Neuro-Oncology* 17.10 (2015), pp. 1322–1332.

[13] C. Chirizzi et al. 'Next-generation agents for fluorescence-guided glioblastoma surgery'. *Bioengineering & Translational Medicine* (2023).

[14] N. F. Marko et al. 'Extent of Resection of Glioblastoma Revisited: Personalized Survival Modeling Facilitates More Accurate Survival Prediction and Supports a Maximum-Safe-Resection Approach to Surgery'. *Journal of Clinical Oncology* 32.8 (2014), pp. 774–782.

[15] J. Falco et al. 'In Silico Mathematical Modelling for Glioblastoma: A Critical Review and a Patient-Specific Case'. *Journal of Clinical Medicine* 10.10 (2021), p. 2169.

[16] G. A. Ateshian. 'On the theory of reactive mixtures for modeling biological growth'. *Biomechanics and Modeling in Mechanobiology* 6 (2007), pp. 423–445.

[17] A. Agosti et al. 'A computational framework for the personalized clinical treatment of glioblastoma multiforme'. *Zeitschrift für Angewandte Mathematik und Mechanik* 98.12 (2018), pp. 2307–2327.

[18] G. Pozzi et al. 'T cell therapy against cancer: A predictive diffuse-interface mathematical model informed by pre-clinical studies'. *Journal of Theoretical Biology* 547 (2022), p. 111172.

[19] A. Agosti et al. 'A personalized mathematical tool for neuro-oncology: A clinical case study'. *International Journal of Non-Linear Mechanics* 107 (2018), pp. 170–181.

[20] H. Garcke et al. 'A Cahn–Hilliard–Darcy model for tumour growth with chemotaxis and active transport'. *Mathematical Models and Methods in Applied Sciences* 26.06 (2016), pp. 1095–1148.

[21] E. A. Swabb, J. Wei and P. M. Gullino. 'Diffusion and convection in normal and neoplastic tissues'. *Cancer Research* 34.10 (1974), pp. 2814–2822.

[22] K. R. Swanson, E. C. Alvord Jr and J. Murray. 'A quantitative model for differential motility of gliomas in grey and white matter'. *Cell Proliferation* 33.5 (2000), pp. 317–329.

[23] A. Martínez-González et al. 'Hypoxic cell waves around necrotic cores in glioblastoma: a biomathematical model and its therapeutic implications'. *Bulletin of Mathematical Biology* 74 (2012), pp. 2875–2896.

[24] C. Chatelain et al. 'Emergence of microstructural patterns in skin cancer: a phase separation analysis in a binary mixture'. *New Journal of Physics* 13.11 (2011), p. 115013.

[25] O. Clatz et al. 'Realistic simulation of the 3-D growth of brain tumors in MR images coupling diffusion with biomechanical deformation'. *IEEE Transactions on Medical Imaging* 24.10 (2005), pp. 1334–1346.

[26] B. Bedogni and M. B. Powell. 'Hypoxia, melanocytes and melanoma–survival and tumor development in the permissive microenvironment of the skin'. *Pigment Cell & Melanoma Research* 22.2 (2009), pp. 166–174.

[27] H. Byrne and L. Preziosi. 'Modelling solid tumour growth using the theory of mixtures'. *Mathematical Medicine and Biology* 20.4 (2003), pp. 341–366.

[28] G. Tierra and F. Guillén-González. 'Numerical methods for solving the Cahn–Hilliard equation and its applicability to related energy-based models'. *Archives of Computational Methods in Engineering* 22 (2015), pp. 269–289.

[29] J. S. Hesthaven, G. Rozza and B. Stamm. *Certified Reduced Basis Methods for Parametrized Partial Differential Equations*. SpringerBriefs in Mathematics. Springer International Publishing, 2015.

[30] A. Quarteroni, A. Manzoni and F. Negri. *Reduced Basis Methods for Partial Differential Equations*. Springer International Publishing, 2016.

[31] C. Audouze, F. De Vuyst and P. B. Nair. 'Reduced-order modeling of parameterized PDEs using time-space-parameter principal component analysis'. *International Journal for Numerical Methods in Engineering* 80.8 (2009), pp. 1025–1057.

[32] M.-L. Rapún and J. M. Vega. 'Reduced order models based on local POD plus Galerkin projection'. *Journal of Computational Physics* 229.8 (2010), pp. 3046–3063.

[33] C. Himpe, T. Leibner and S. Rave. 'Hierarchical approximate proper orthogonal decomposition'. *SIAM Journal on Scientific Computing* 40.5 (2018), A3267–A3292.

[34] Q. Wang, J. Hesthaven and D. Ray. 'Non-intrusive reduced order modeling of unsteady flows using artificial neural networks with application to a combustion problem'. *Journal of Computational Physics* 384 (2019), pp. 289–307.

[35] A. Agosti et al. 'Learning patient-specific parameters for a diffuse interface glioblastoma model from neuroimaging data'. *Mathematical Methods in the Applied Sciences* 43.15 (2020), pp. 8945–8979.

[36] S. Chaturantabut and D. C. Sorensen. 'Nonlinear Model Reduction via Discrete Empirical Interpolation'. *SIAM Journal on Scientific Computing* 32.5 (2010), pp. 2737–2764.

[37] J. Hesthaven and S. Ubbiali. 'Non-intrusive reduced order modeling of nonlinear problems using neural networks'. *Journal of Computational Physics* 363 (2018).

[38] D. C. Liu and J. Nocedal. 'On the limited memory BFGS method for large scale optimization'. *Mathematical Programming* 45.1 (1989), pp. 503–528.

[39] G. L. Celora et al. 'Phenotypic variation modulates the growth dynamics and response to radiotherapy of solid tumours under normoxia and hypoxia'. *Journal of Theoretical Biology* 527 (2021), p. 110792.

[40] D. Ambrosi and F. Mollica. 'On the mechanics of a growing tumor'. *International journal of engineering science* 40.12 (2002), pp. 1297–1316.

[41] R. K. Jain, J. D. Martin and T. Stylianopoulos. 'The role of mechanical forces in tumor growth and therapy'. *Annual review of biomedical engineering* 16.1 (2014), pp. 321–346.

[42] D. Riccobelli. 'Elastocapillarity-driven surface growth in tumour spheroids'. *arXiv preprint arXiv:2410.03344* (2024).

[43] T. Lassila and G. Rozza. 'Parametric free-form shape design with PDE models and reduced basis method'. *Computer Methods in Applied Mechanics and Engineering* 199.23-24 (2010), pp. 1583–1592.

[44] A. Manzoni, A. Quarteroni and G. Rozza. 'Model reduction techniques for fast blood flow simulation in parametrized geometries'. *International Journal for Numerical Methods in Biomedical Engineering* 28.6-7 (2012), pp. 604–625.

[45] L. Zhang et al. 'Shape-informed surrogate models based on signed distance function domain encoding'. *arXiv preprint arXiv:2409.12400* (2024).

[46] F. Acerbi et al. 'Mechano-Biological Features in a Patient-Specific Computational Model of Glioblastoma'. In: *Neuromethods*. Springer US, 2020, pp. 265–287.

[47] N. Sanai and M. S. Berger. 'Operative Techniques for Gliomas and the Value of Extent of Resection'. *Neurotherapeutics* 6.3 (2009), pp. 478–486.

[48] M. Weller et al. 'European Association for Neuro-Oncology (EANO) guideline on the diagnosis and treatment of adult astrocytic and oligodendroglial gliomas'. *The Lancet Oncology* 18.6 (2017), e315–e329.

MOX Technical Reports, last issues

Dipartimento di Matematica
Politecnico di Milano, Via Bonardi 9 - 20133 Milano (Italy)

103/2024 Fois, M.; Gatti, F.; de Falco, C.; Formaggia, L.
A comparative analysis of mesh-based and particle-based numerical methods for landslide run-out simulations

102/2024 Bucelli, M.
The lifex library version 2.0

101/2024 Bonetti, S.; Corti, M.
Unified discontinuous Galerkin analysis of a thermo/poro-viscoelasticity model

100/2024 Farenga, N.; Fresca, S.; Brivio, S.; Manzoni, A.
On latent dynamics learning in nonlinear reduced order modeling

99/2024 Ragni, A.; Masci, C.; Paganoni, A. M.
Analysis of Higher Education Dropouts Dynamics through Multilevel Functional Decomposition of Recurrent Events in Counting Processes

98/2024 Castiglione, C.; Arnone, E.; Bernardi, M.; Farcomeni, A.; Sangalli, L.M.
PDE-regularised spatial quantile regression

97/2024 Ferro, N.; Mezzadri, F.; Carbonaro, D.; Galligani, E.; Gallo, D.; Morbiducci, U.; Chiastra, C.; Perotto, S.
Designing novel vascular stents with enhanced mechanical behavior through topology optimization of existing devices

93/2024 Conti, P.; Kneifl, J.; Manzoni, A.; Frangi, A.; Fehr, J.; Brunton, S.L.; Kutz, J.N.
VENI, VINDy, VICI - a variational reduced-order modeling framework with uncertainty quantification

95/2024 Zacchei, F.; Rizzini, F.; Gattere, G.; Frangi, A.; Manzoni, A.
Neural networks based surrogate modeling for efficient uncertainty quantification and calibration of MEMS accelerometers

96/2024 Brivio, S.; Fresca, S.; Manzoni, A.
PTPI-DL-ROMs: Pre-trained physics-informed deep learning-based reduced order models for nonlinear parametrized PDEs